Investigation into the Competitive and Site-Specific Nature of Anion Adsorption on Pt Using In Situ X-ray Absorption Spectroscopy

Thomas M. Arruda,[†] Badri Shyam,[‡] Joseph M. Ziegelbauer,[†,§] Sanjeev Mukerjee,*[,†] and David E. Ramaker[‡]

Department of Chemistry and Chemical Biology, Northeastern University, Boston, Massachusetts 02115, and Department of Chemistry, George Washington University, Washington, D.C. 20052

Received: July 29, 2008; Revised Manuscript Received: September 4, 2008

In situ X-ray absorption spectroscopy along with electrochemical measurements (CV and RDE) and previously published EQCN data provide further understanding of the nature of chloride poisoning on different faces/sites of carbon supported platinum clusters (1−2 nm) in acidic medium ($HClO_4$). Chloride is shown to adsorb in 3-fold sites on the Pt(111) faces at the investigated Cl^- concentrations (10^{-3} and 10^{-2} M). Atop chloride was found to be present within a narrow potential range (0.4−0.7 V RHE) when compressed adlayers of Cl^- are formed on the Pt(111) faces forcing some Cl^- to exist in atop/bridged sites. The interplay of anionic (Cl^-, Br^-, OH^-, and HSO_4^-) adsorption on the different surfaces of Pt are also considered. For example O/OH can easily displace atop chloride on the edges/corners but not the Cl^- at the Pt(111) sites, and therefore Cl^- dramatically raises the overpotential for water activation at the Pt(111) sites. Chloride also drastically alters the ORR causing an increase of the overpotential by ∼85 mV for every 10-fold increase in chloride concentration with a total 150−200 mV increase in the overpotential at large concentrations at the Pt(111) sites. Finally Cl^- ions cannot displace the bisulfate overlayer on the Pt(111) faces after it is formed at lower potentials; however, once the bisulfate adsorption is disturbed at higher potentials, the bisulfate cannot displace the Cl^- adsorption. These relative anion adsorption preferences can help to explain the different dependencies of the important ORR on anion adsorption, and suggests that the effect of Cl^- poisoning might be quite dependent on the Pt particle size.

Introduction

Highly dispersed polycrystalline platinum nanoparticles are still considered to be the premier electrocatalysts for use in low and medium temperature fuel cells such as polymer electrolyte membrane fuel cells (low temperature, PEMFC) and the acid-imbibed analogues (medium temperature PBI-Phosphoric acid based). They are also candidates for potential applications in new hybrid concepts as reversible electrodes for large scale energy storage using modified flow-through battery configurations. To date they still exhibit the highest activity toward the oxygen reduction reaction (ORR) and are relatively resistant to corrosion under standard fuel cell operating conditions. When used as an anode, platinum demonstrates near perfect electrokinetics as the overpotential of hydrogen oxidation/evolution is negligible in pure, hydrated H_2 streams.[1] The high activity exhibited by Pt is also the reason for its higher susceptibility to poisoning by species which have higher chemisorption ability. One of the significant classes of such surface poisons are halides.

Due to the aforementioned importance of platinum and its susceptibility to poisoning, a myriad of studies on Pt poisoning have been published over the years. Many of these endeavors have investigated the adsorption of anions such as bisulfate and halides revealing adverse electrochemical effects.[2−9] In the presence of strongly adsorbing anions, ORR on platinum suffers further overpotential losses of several hundred millivolts beyond that due to the sluggish ORR kinetics in clean electrolytes.[10,11] In addition, H_2O_2 byproduct formation has been shown to increase in the presence of adsorbed anions.[10] The presence of H_2O_2 in a fuel cell electrode−electrolyte interface is known to lead to formation of free radicals such as hydroxyl and peroxy-hydroxyl which ultimately attack the polymer electrolyte membrane, causing durability issues.[12] It is generally accepted that the adsorption strength of adsorbed halides on platinum increases in the order $Cl^- < Br^- < I^-$.[5] The reversibility of halide adsorption, however, has been somewhat controversial. Lane et al.[13] suggested that halides adsorb strongly enough to withstand rinsing with an inert electrolyte. Such irreversibility however has been contradicted by subsequent investigations employing radiotracers to demonstrate dislodgement of adsorbed Cl^- by other halides or rinsing with clean electrolyte.[3]

Halide poisoning is commonly observed during cyclic voltammetry (CV); one such example in acidic and alkaline media revealed significant alteration of the H underpotential deposition (H_{upd}) peaks particularly with respect to amplitude and position in platinum CVs.[4] This suggested chloride anions were present on the platinum surface even at low potentials. Other studies have demonstrated halide anion influences at concentrations as low as μM levels.[2,3] In the context of O[H] adsorption from water activation, adsorbed halide anions were shown to frustrate Pt−O[H] formation as indicated by the anodic peak suppression/shift in the CV.[10] Further Rotating Ring Disk Electrode (RRDE) measurements also revealed an increased production of H_2O_2 on Pt(100) facets.[10] The competitive nature of O[H] and Cl^- adsorption was probed by chronocoulometric measurements.[14]

* To whom correspondence should be addressed. E-mail: s.mukerjee@neu.edu.
[†] Northeastern University.
[‡] George Washington University.
[§] Current address: General Motors Research and Development Center, M/C: 480-102-000, 30500 Mound Rd., Warren, MI 48090.

10.1021/jp8067359 CCC: $40.75
Published on Web 10/29/2008

Thermodynamic analyses of the charge density was used to determine the Gibbs energy of adsorption (142 kJ mol^{-1} Cl^-, 136 kJ mol^{-1} O[H] on Pt(111)), suggesting that the coexistence of Cl^- and O[H] inhibited the development of an ordered Cl^- adlayer.

Since anion adsorption is a surface phenomenon, most of the available surface sensitive techniques have been exploited to elucidate adsorbate coverage and structure. Such techniques include auger electron spectroscopy (AES), low energy electron diffraction (LEED), second harmonic generation (SHG) and surface X-ray scattering (SXS), all of which revealed significant results. Through AES/LEED studies, it was determined that Cl_{ads} occurs on Pt(100) and Pt(111) surfaces in two separate electrochemical windows; the hydrogen desorption region and the onset of O[H] adsorption region.[15] The Pt(100) surface was also shown to be affected by Cl^- at a lower potential than Pt(111) indicating Pt(100) was more susceptible to Cl^- poisoning. SHG experiments indicate a strong correlation between halide concentration and monolayer coverage (0.1 ML to >0.9 ML for Cl^- concentration of $10^{-6}-10^{-4}$ M, respectively).[16] Similar findings were obtained for Br^- anions adsorbed on platinum. Modern X-ray scattering methods have also proved invaluable for surface studies. For example, Marković et al.[5,17] established that Cl^- adsorbs on platinum with a Pt−Cl interatomic separation of 2.4Å with no ordered, in-plane structure. Analysis of crystal truncation rods (CTR) in the above studies yielded a monolayer coverage of 0.6 ML at 0.7 V vs reversible hydrogen electrode (RHE) with a Pt−Cl interatomic distance of approximately 2.4 Å. Interatomic Cl−Cl distances were also determined to be in the range of 3.58−4.39 Å at 0.7 and 0.25 V, respectively.

As mentioned above, the spectroscopic methods used to study anion adsorption have revealed pertinent fundamental information; however, most methods are either dependent on ultra high vacuum conditions (UHV) or have been employed on single crystals. Such results may not be comparable to in operando fuel cell catalyst surfaces, which are polycrystalline in nature and strongly influenced by their surroundings, such as the presence of electrolyte or gases. In order to obtain a more complete description of the catalyst surface, in situ experiments should be employed on actual fuel cell materials.

Over the past two decades X-ray absorption spectroscopy (XAS) has been developed into a reliable method to study electrode processes in situ via extended X-ray absorption fine structure (EXAFS) and X-ray absorption near edge structure (XANES).[18−20] Because of the high photon flux of modern day synchrotron sources, XAS is available to probe materials in situ without significant X-ray beam attenuation. XAS allows for the determination of bond distances, coordination numbers, mean-square-disorder term (commonly referred to as Debye−Waller factor) and oxidation state without the necessity of long-range order. When acquired in situ, the above parameters can be evaluated under operating fuel cell conditions. Historically, the inherent bulk averaging nature of XAS has limited its utility for surface studies. Recently however, the delta mu ($\Delta\mu$) method of XANES analysis has been developed as a surface sensitive method to determine surface/adsorbate interactions.[21−24] The $\Delta\mu$ analysis isolates surface/adsorbate interactions by subtracting out the bulk metal−metal interactions. Once obtained, the $\Delta\mu$ spectra are compared to theoretical $\Delta\mu$ curves generated based on crystallographic models.

Water activation studies utilizing Pt L_3 edge XANES data in acidic media have revealed that OH_{ads} on platinum occurs in an atop configuration (1-fold) at low potentials, followed by 2- and 3-fold symmetries with increasing electrode polarization until finally place exchange occurs at 1.05V and higher.[25−27] Prior to these studies it was believed that place exchange occurred only at potentials greater than 1.2V. The $\Delta\mu$ technique was also employed to investigate hydrogen adsorption and mobility on platinum catalysts in the UPD region of the platinum CV.[28,29] At low coverage, H was found to be delocalized on the platinum surface, while at higher coverage, H occupied fcc sites as well as edge/step locations. Other platinum based in situ XAS systems that have been explored utilizing the $\Delta\mu$ technique include bisulfate poisoning of platinum,[30] and CO_{ads} on PtRu alloy electrocatalysts.[31] The $\Delta\mu$ technique was also applied to a nonmetallic, heterogeneous (3-phase) Rh_xS_y system to examine H_2O activation.[32] After a complex analysis of Rh_xS_y clusters, it was established that O adsorbs in one-fold sites at low potentials and bridge-bonded sites at 0.8 V and above. This XAS investigation also identified the Rh_3S_4 moiety as the electroactive phase of the heterogeneous Rh_xS_y material when the previous inclination was that $Rh_{17}S_{15}$ was the active phase.

Previously, we determined the Cl^- poisoning site on Pt in Cl^- contaminated electrolytes by using the $\Delta\mu$ method.[33] In this work we extend our study to include a detailed analysis of Cl^- adsorption on all low index Pt faces, corner, and edge sites using both electrochemical and spectroscopic methods. Through in situ XAS measurements ($\Delta\mu$ technique and EXAFS) we are able to show that Cl^- anions affect water activation differently depending on binding site. There is also a Cl^- anion concentration effect which is apparent over the concentration range we study. Further, the $\Delta\mu$ technique provides an atomic level view of the surface−adsorbate interactions, which allows us to determine the adsorption site of Cl^- on a polycrystalline Pt/C electrocatalyst.

Experimental Section

Electrochemical Characterization. RDE studies were performed as described in detail elsewhere.[25] Briefly, inks of 30 wt % Pt/C (Vulcan XC72 from E-TEK) were prepared by combining 10 mg catalyst, 5 mL deionized water (18.2MΩ, Millipore MilliQ system), 5 mL 2-propanol (HPLC grade, Aldrich), and 40 μL 5 wt % Nafion solution (Aldrich). The ink was then sonicated for 15 min and stirred for 2 h. The ink was then cast onto a polished glassy carbon (GC) RDE (Pine Instrument Co.) via two 5 μL aliquots, and allowed to dry in air after each application. The final metal loading on the GC was 14 μg cm^{-2} Pt. The corresponding Nafion to catalyst ratio was 1:50 by weight. Room temperature CVs were obtained in 1 M $HClO_4$ (GFS Chemicals, doubly distilled), 1 M $HClO_4$ + 10^{-3} M KCl (Aldrich, 99.999% pure) and 1 M $HClO_4$ + 10^{-2} M KCl under an Ar (Med-Tech Gasses) atmosphere. For oxygen reduction experiments the above electrolytes were purged with ultra high purity O_2. All data were collected with an Autolab potentiostat (model PGSTAT30, Ecochemie-Brinkmann). For all of the experiments a sealed RHE, filled with 1 M $HClO_4$ was utilized as the reference electrode and a high surface area Pt mesh (Alfa Aesar) functioned as the counter electrode. All current densities reported in this text refer to geometric surface area as the poisoning effects of chloride render H_{upd} adsorption useless for surface area measurements. As reported earlier,[34] average particle size of these electrocatalysts were in the range of 1–2 nm.

In Situ XAS Data Collection. All experiments were conducted at room temperature in an in situ electrochemical XAS cell based on a previously reported design.[35] The cells used consisted of a 30 wt% Pt/VXC72 (*E-TEK*) working electrode

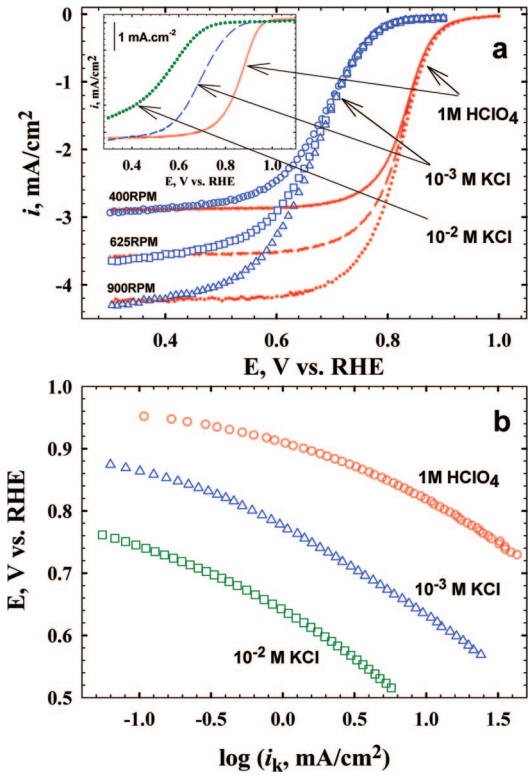

Figure 1. (a) ORR polarization curves (anodic sweep) for 30 wt % Pt/C on a glassy carbon disk in O_2 saturated 1 M $HClO_4$ and 1 M $HClO_4$ + 10^{-3} M KCl at 20 °C using a sweep rate of 20 mV s^{-1}. The inset includes 1 M $HClO_4$ + 10^{-2} M KCl (dotted); (b) Mass transfer corrected Tafel plots taken at 900 RPM for 30 wt % Pt/C in 1 M $HClO_4$ (circles), 1 M $HClO_4$ + 10^{-3} M KCl (triangles), and 1 M $HClO_4$ + 10^{-2} M KCl (squares). All current densities utilize geometric surface area.

(WE), an acid washed (0.5 M H_2SO_4) Grafoil counter electrode (CE) and an RHE reference electrode. The WE and CE were separated by a piece of Nafion 112 (DuPont) polymer electrolyte membrane and the cell was flooded with 1 M $HClO_4$ + xM KCl (x = 10^{-3} or 10^{-2} M). Grafoil was chosen as a CE to eliminate any interference at the Pt $L_{3,2}$ edges with little X-ray beam attenuation and $HClO_4$ was utilized for its low anion adsorption effects on platinum. In all cases, Au wire (99.999%, Alfa-Aesar) was utilized as a current collector and mechanically pressed against the back side of the electrode in a fashion which did not expose the gold to the X-ray beam. Silicone gaskets (Auburn Chemical Co.) were used to seal the cell. The electrodes were prepared by hand painting catalyst suspensions of 30 wt % Pt/VXC72, 1:1 deionized H_2O/2-propanol mixture and 95:5 mixture of catalyst (wt)/5 wt % Nafion solution. The inks were painted onto commercially available carbon cloth (Zoltek) with a loading of ~5 mg cm^{-2} Pt to obtain an absorption cross section of ~1. The total geometric area of the Pt WE used in the cell was 5 cm^2. To ensure proper electrode wetting, each electrode was vacuum impregnated in clean electrolyte prior to cell assembly.

The platinum working electrodes were activated by potential cycling (0.05 to 1.2 V vs RHE at 10 mV s^{-1}) in clean 1 M $HClO_4$. Following the activation step, the clean electrolyte was removed from the cell by syringe and replaced with 1 M $HClO_4$ + xM KCl (x = 0, 10^{-3}, 10^{-2}). Full range Pt L_3 extended X-ray absorption fine structure (EXAFS) were taken (−250 eV to 18k) with the WE fixed at various static potentials along the anodic sweep of the CV. Between EXAFS scans the potential was cycled around completely to 'clean' the electrode surface. A full set of EXAFS were also obtained in clean 1 M $HClO_4$ to provide clean reference scans and as H_2O activation standards. The measurements were performed at beam line X11-B (National Synchrotron Light Source, Brookhaven National Laboratory, Upton, NY) with the Si(111) monochromator detuned by 40% in order to reject the higher harmonics from the beam. Data were collected in transmission mode using gas ionization detectors (I_0, I_1 or I_2) with a nominal nitrogen/argon gas mixture to allow ~10% photon absorption in I_0 and 70% in I_1. The sample was placed between the I_0 and I_1 detectors, while a Pt reference foil (4 μm, Alfa Aesar) was positioned between I_1 and I_2.

EXAFS and $\Delta\mu$ Analysis. The IFEFFIT suite[36] (version 1.2.9, IFEFFIT Copyright 2005, Matthew Newville, University of Chicago, http://cars9.uchicago.edu/ifeffit/) was utilized for background subtraction (AUTOBK)[37] and normalization. A k-range window of 1.988−14.072 Å^{-1} (Kaiser-Bessel) and an R-window of 1.532−3.379 Å were used for all the EXAFS fits.

Alignment and Normalization of XAS Data. The $\Delta\mu$ analysis technique has been described in great detail elsewhere.[22,24,38,39] Briefly, XAS reference scans were carefully calibrated to the edge energy (11564 eV, Pt L_3) and aligned to one standard reference scan as the beam energy is known to "drift" over the duration of the beam lifetime (12 h.). Any edge shift corrections applied to the reference foils are automatically applied to their respective sample scans. A postedge normalization procedure was then applied to the aligned scans via a cubic spline function (AUTOBK)[37] which normalizes the oscillations over a specific energy range (for Pt $\Delta\mu$ typically 25−150 eV with respect to E_0, 150−1000 eV for EXAFS) to present the data on a per-atom basis. These parameters often vary from scan to scan and are assessed on an individual basis.[39] Difference spectra were constructed using the equation

$$\Delta\mu = \mu(\mathrm{V}) - \mu(0.54\ \mathrm{V}) \quad (1)$$

where μ(V) is the sample at various potentials and μ(0.54) is the reference signal at 0.54 V, which is considered the cleanest region of platinum; i.e., relatively free of any adsorbed H, OH or O_x species. The $\Delta\mu$ spectra are then compared to theoretical curves ($\Delta\mu_t$) constructed using the FEFF 8.0 code. This was accomplished using the relationship

$$\Delta\mu_t = \mu(\mathrm{Pt_6X}) - (\mathrm{Pt_6}) \quad (2)$$

where X is Cl^- or O in a specified binding site with respect to the absorbing Pt atom and Pt_6 is a six-Pt cluster with a Pt−Pt bond distance of 2.77 Å as described by Janin et al.[40] It should be noted that theoretical $\Delta\mu$ curves are generally shifted by 1−5 eV and scaled by a multiplication factor for optimal comparison with experimental data.

Results and Discussion

Electrochemical Characterization. As mentioned above, the presence of Cl^- anions severely impedes the oxygen reduction reaction (ORR) on Pt/C electrocatalysts. Figure 1a presents the rotating disk electrode (RDE) curves for Pt/C in clean and Cl^- contaminated electrolyte at several rotation rates. In clean electrolyte a reasonable ORR activity is observed with an onset potential close to 1.0 V vs RHE. In addition, a well defined diffusion limiting current is obtained as a function of rotation rate as described by the Levich equation:

$$i_{\mathrm{lim}} = 0.62 n_e F D^{2/3} \nu^{-1/6} C_o \quad (3)$$

where i_{lim} is the diffusion limiting current density, n_e is the number of electrons, F is Faraday's constant, D is the diffusion

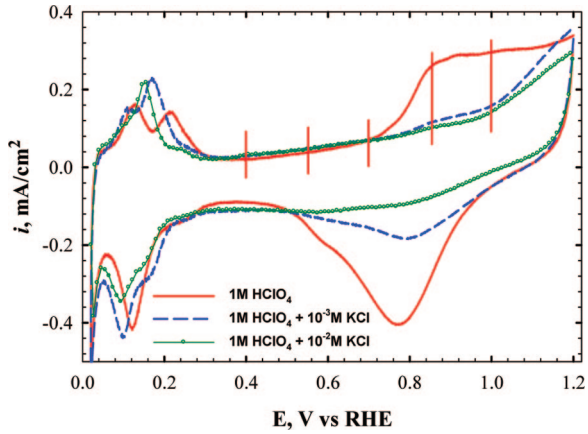

Figure 2. CVs of 30 wt % Pt/C (*E-TEK*) in Ar-saturated 1 M $HClO_4$ (solid), 1 M $HClO_4$ + 10^{-3} M KCl (dashed) and 1 M $HClO_4$ + 10^{-2} M KCl (dotted) with a scan rate of 50 mV s^{-1} on a 5 mm glassy carbon RDE tip at 0 RPM. The vertical lines indicate potentials at which EXAFS measurements were made.

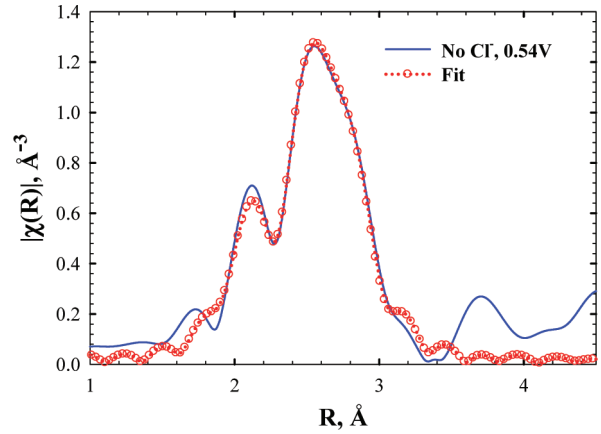

Figure 3. Fourier transformed EXAFS for 30 wt % Pt/C in 1 M $HClO_4$ at 0.54 V vs RHE measured in situ at the Pt-L_3 edge. Phase and amplitude parameters were fit using those generated with IFEFFIT 1.2.9 and sample data. Single shell (Pt−Pt) fit, ($1.5 < k < 15.8$ $Å^{-1}$, k^2 weighted), performed in *R*-space.

coefficient of O_2 in the electrolyte, ν is the kinematic viscosity and C_o is the concentration of O_2. With each 10-fold addition of chloride, the ORR overpotential is increased by ~85 mV with respect to the curve in 1 M $HClO_4$. Though the Levich relationship still appears to exist, a clear delineation of a diffusion limiting current is less evident in the presence of Cl^-. This is more manifest for ORR with 10^{-2} M chloride concentration (dotted line, inset). At this concentration a significant change in the magnitude of the limiting current is observed. The Tafel plots shown in Figure 1b were extracted from the ORR polarizations (anodic scan) following a correction for mass transport by the equation

$$i_k = i_{lim} \times i/(i_{lim} - i) \quad (4)$$

where i_k is the kinetic current density, i_{lim} is the diffusion limiting current as described by eq 3 and i is the measured current during the ORR polarization. The anodic scan was used since this represents the ORR activity initiated on a relatively clean Pt surface with the competing effects of Cl^- and oxide growth as a function of positive potential scan. The cathodic scan proceeds with a pre-existing oxide covered surface, thereby representing a more complex kinetic analysis perspective. Though it was mentioned above that Cl^- contamination resulted in the loss of a well-defined diffusion limiting current, we utilize the current density at 0.3 V in each electrolyte as i_{lim} to maintain consistency. The overall shape of the Tafel curves remain relatively unchanged with chloride present, indicating no significant change in the rate limiting step of ORR. The decrease in electrocatalytic activity reflects the increased overpotentials caused by Cl^-, and is consistent with a site blocking mechanism.[10,41] These observations agree with work recently reported by Schmidt et al.[10] Although their work was done at elevated temperature (60 °C) and with a slower sweep rate (5 mV s^{-1}), they observed similar overpotentials as a function of chloride concentration.

To further illustrate the effect of chloride adsorption on platinum, cyclic voltammograms with and without chloride are presented in Figure 2. The solid line representing polycrystalline platinum in clean $HClO_4$ reveals all the signature platinum features. Perhaps the most notably are Pt−O[H] formation (anodic sweep, >0.70 V) and reduction (cathodic sweep, ca. 0.80 V). From inspection of the chloride contaminated voltammograms (dashed 10^{-3} M, dotted 10^{-2} M), it is evident that adsorbed Cl^- hinders O[H] adsorption at 0.70 V. It is not until the electrode is polarized to approximately 1.0 V that an appreciable increase in current density is attained, whence Pt−O formation occurs despite the chloride presence. This delay in the onset potential for O[H] adsorption has been confirmed by earlier studies on both single crystals[5,42−44] and polycrystalline Pt.[10,45,46] Though it is not the objective of this work to investigate the effect of chloride on H_{upd}, it is worth mentioning that changes in H_{upd} peaks are also observed. Among the halides, I^- adsorption is known to be the strongest,[2,10] and thus affects the H_{upd} region to a much larger extent, and in a very different manner than either Cl^- or Br^-. The adsorption of Cl^- is known to take place on at least three distinct sites (2 for Br) with differing energies of activation. This however does not change the total amount of adsorbed hydrogen. The potential range over which H_{ads} occurs is also reduced in the presence of halides and is generally recognized to be due to the competitive nature of the adsorbed ions on the Pt surface. There is also evidence in the literature for the partial desorption of Cl^- and Br^- in this region. Such phenomena, however, have already been adequately explained[2,9] and thus will not be discussed here in further detail.

EXAFS Results. Prior to the $\Delta\mu$ XANES analysis, traditional Fourier Transform (FT) EXAFS analysis was performed to ensure no major changes in Pt−Pt bond length occur as a function of potential. Such changes would yield unreliable results as $\Delta\mu$ relies on crystallographic modeling with consistent bond lengths to generate theoretical $\Delta\mu$ signatures. To elucidate quantitative structural information, the EXAFS data were fit using Artemis, a subroutine of the IFEFFIT code.[36] A representative fit is presented in Figure 3 for Pt/C in clean 1 M $HClO_4$ at 0.54 V vs RHE. In this region no adsorbed species (such as hydrides or oxides) are expected and therefore it is generally representative of a clean metal surface. The fit utilized a single shell Pt−Pt scattering path to isolate the effect that adsorbates exhibit on local Pt structure. Table 1 offers a summary of the EXAFS fitting parameters for the Pt L_3 edge in each electrolyte as a function of electrode potential in the range between 0.4 and 1.00 V vs RHE. As evidenced by the *R* values, no major changes in bond length occur although the coordination number (*N*) is altered as a function of potential representing the effect of adsorbed species (both Cl^- and oxides). In order to include the Pt−Cl and Pt−O interactions, corresponding 3 shell fits were conducted (Pt−Pt, Pt−Cl and Pt−O), however for simplicity only the Pt−Pt interactions are shown in Table 1. It should be

TABLE 1: Summary of EXAFS Results[a]

potential (V, RHE)	N_{Pt-Pt} $\Delta N = \pm 0.4$[b]	R_{Pt-Pt} (Å) $\Delta R = \pm 0.035$[b]	E_0 (eV) $\Delta E_0 \pm 1.50$	σ^2 (Å^2)
		1 M $HClO_4$		
0.40	8.9	2.74	8.99	0.0065
0.54	9.1	2.74	8.99	0.0065
0.70	9.1	2.74	8.94	0.0065
0.84	9.2	2.74	8.78	0.0065
1.00	8.8	2.74	8.91	0.0065
		1 M $HClO_4$ + 10^{-3} M KCl		
0.40	8.7	2.73	9.08	0.0065
0.54	8.8	2.73	8.86	0.0065
0.70	8.8	2.74	8.83	0.0065
0.84	9.0	2.74	8.88	0.0065
1.00	8.4	2.74	8.59	0.0065
		1 M $HClO_4$ + 10^{-2} M KCl		
0.40	7.6	2.74	9.35	0.0065
0.54	7.9	2.74	9.23	0.0065
0.70	7.2	2.74	9.75	0.0065
0.84	7.5	2.74	9.77	0.0065
1.00	7.0	2.74	9.46	0.0065

[a] S_0^2 fixed at 0.934 as calculated by FEFF8.0. [b] Although the absolute values of ΔN and ΔR are larger than those indicated, the variation of N and R with potential is believed to be meaningful down to the values indicated.

noted that the Pt−Cl bond lengths[17] of ∼2.4 Å were very difficult to resolve from the Pt−Pt path, which is located between 2.3 and 2.6 Å.

The EXAFS results obtained in 1 M $HClO_4$ were used to determine the average bulk Pt−Pt coordination number (N_{Pt-Pt}) which was determined to be in the range of 8 and 9. From these results, the Pt/C nanoparticles can be estimated to be between 1 and 1.5 nm in diameter,[47] with a dispersion factor of around 50−60%,[48] and thereby consisting of ∼55−150 atoms.[5] These were calculated using algorithms developed earlier by Benfield.[49] These algorithms provide an important link between the geometric models of clusters described by Hardeveld and co-workers[50,51] and the shell-by-shell approach used in EXAFS analysis. Accordingly, the cubooctahedron model of Benfield[49] was used in this analysis, although different from those used previously by Kinoshita[48] and Stonehart,[52] which estimate a much higher ratio of 111/100 facets (see columns 7 and 8 of Table 2). The latter is apparently better for smaller particles, when the lower surface energy of the 111 facets compared to the 100 facets makes the 111 facets preferred. Results from the cluster analysis are shown in Table 2 for various cluster sizes in the range of 10−60 Å. The most reactive sites are those which correspond to low surface coordination numbers. These are depicted in Table 2 in terms of the fraction of surface atoms at vertices (N_{vertex}), edges (N_{edge}), and 111 or 100 faces. When compared to the number of sites on bulk crystallographic planes such as the Pt(100), Pt(111) faces, the edges and steps predominate below 15 Å. However, with the particle size greater than 20 Å, the bulk crystallographic planes assume importance. From our previous study on the effect of particle size on electrocatalysis,[53] it is clear that the predominance of low coordination sites, such as the edge and steps, are detrimental to the ORR activity. This was based on in situ XAS investigations of a series of Pt/C electrocatalysts with varying particle sizes.[53] The XAS data in this prior study showed unequivocally that the imbalance of charge on the edge and step sites in these small clusters below 20 Å results in the strong adsorption of both hydrides and oxides on the Pt surface (depending on the potential region it is exposed to) thereby rendering the surface largely inactive for electrocatalysis. A visual representation of the variation of the population of various surface crystal faces as a ratio to the total number of surface atoms is expressed as a plot with respect to overall particle size in Figure 4.

To visualize the effect of Cl^- on Pt clusters, the Pt coordination numbers tabulated in Table 1 are plotted in Figure 5. Without Cl^- present, N_{Pt-Pt} is observed decreasing at low and high potentials. The former has been explained[29] by the desorption of H^+ from the surface while the latter is attributed to the formation of Pt−O_x species.[27] In general, adsorbed H^+ (and other species in atop positions) tend to make the cluster more spherical, which increases N by increasing the bulk to surface character of the clusters. Conversely, adsorbed species in 3-fold positions tend to decrease N, similar to that indicated for O_x and as we will show with $\Delta\mu$ for Cl^-. In the presence of Cl^- there is a noticeable decrease in bulk N_{Pt-Pt} with the effect compounded as [Cl^-] is increased. In 10^{-2} M Cl^- the general downward trend in N_{Pt-Pt} is observed, however, with some unexpected 'bumps' not observed in the other electrolytes. Such phenomena are complex and will be explained in detail later.

It is also interesting to note that the increase in chloride concentration has little or no effect on the rate of change (i.e., the negative slope) of N_{Pt-Pt} in Figure 5 above 0.95 V. Subsurface oxygen is known to form on Pt above 1.00 V, reducing the Pt−Pt scattering sharply.[27] Since the oxygen that goes subsurface is actually the oxygen that was previously adsorbed at lower potentials, adsorbed chloride is not expected to hinder the movement of these oxygen atoms and therefore the rate of change in N_{Pt-Pt} is not significantly affected.

$\Delta\mu$ Results. Figure 6 shows the $\Delta\mu$ spectra for the Pt/C electrodes fixed at the indicated potentials (0.4−1.0 V vs RHE). The spectra in Figure 6a indicate a normal H_2O activation pathway for platinum in $HClO_4$. In the potential region where Pt-OH formation occurs, typically 0.7 V, a small positive peak is obtained in the $\Delta\mu$ spectrum near the absorption edge energy. Subsequently, as the potential is increased, the peak increases in both magnitude and energy. This signature change is consistent with a previous report[27] which described it as a transition from atop OH (ca. 0.7 V) to n-fold O ($n = 2$ or 3, typically indistinguishable). Teliska et al.[27] ran $\Delta\mu$ simulations as described by eq 2, using the same Pt_6 clusters employed in this work, with O situated in 1-, 2-, 3- and 4-fold locations. As the Pt−O coordination increased from 1 to 4, the $\Delta\mu$ lines were observed behaving as described above. These line shapes were confirmed as they correlated very well with their in situ $\Delta\mu$ taken in 0.1 M $HClO_4$. Due to the weak scattering properties of H, the $\Delta\mu$ technique cannot distinguish directly between OH and O adsorption; however, DFT calculations[40,54,55] have shown that OH prefers 1-fold coordination (atop) and O prefers 3-fold and therefore the $\Delta\mu$ can indirectly distinguish the two because of their adsorption site preference. The physical basis of these signatures have also been presented in detail earlier.[27] Briefly, the spectral shape of the Pt–O scattering is remarkably unchanged with repect to the binding site. In contrast, the change in Pt−Pt scattering varies significantly with binding site. The change in magnitude and shift to lower energy with increasing N_{Pt-O} is attributed to the weakening of the Pt−Pt interactions due to the formation of multicoordinated, subsurface Pt−O. This is referred to as "d-orbital frustration"[56] resulting from lower Pt−Pt scattering under a weakened Pt–O binding condition as compared to the pristine case.

The $\Delta\mu$ in Figure 6b (10^{-3} M Cl^-) exhibits several additional features not present in the clean $HClO_4$. A consistent negative contribution near 0 eV precedes the Pt−O[H] lines at all

TABLE 2: Distribution of Surface Sites in a Cubo-octahedral Pt Cluster as a Function of Particle Size as Estimated by Benfield[49a]

particle size (Å)	total no. of atoms	N_{surf}/N_{tot}	N_{vertex}/N_{surf}	N_{edge}/N_{surf}	N_{111}/N_{surf}	N_{100}/N_{surf}	N_{111}/N_{surf}[a]	N_{100}/N_{surf}[a]
5.50	13	0.92	1.0	0.00	0.0	0.0	0.0	0.0
11.75	55	0.76	0.29	0.57	0.0	0.14	0.30	0.01
16.28	147	0.63	0.13	0.52	0.09	0.26	0.40	0.03
20.86	309	0.52	0.07	0.44	0.15	0.33	0.56	0.08
30.05	561	0.39	0.05	0.38	0.19	0.38	0.58	0.09
40.00	923	0.30	0.03	0.33	0.22	0.41	0.65	0.12
53.00	1415	0.24	0.02	0.29	0.24	0.44	0.68	0.14

[a] Estimates from Kinoshita.[48]

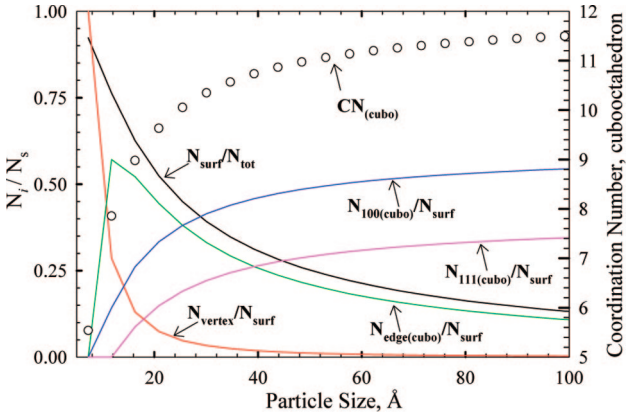

Figure 4. Variation of the ratio of population of various coordination sites on the surface of clusters and the total number of surface sites as a function of the particle size of the cluster. Calculations were performed using the methodology developed by Benfield.[49] Also shown for comparison is the evolution of the total coordination number and those of the individual sites. All calculations were made using a cuboctahedron model cluster.

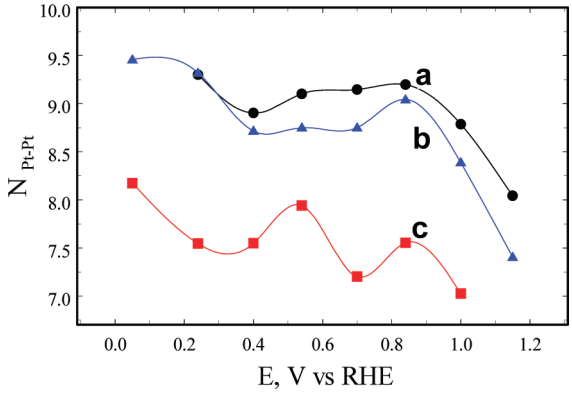

Figure 5. EXAFS results showing change in Pt−Pt coordination as a function of electrode potential for Pt/C electrocatalyst in (a) clean 1 M $HClO_4$, (b) 1 M $HClO_4$ + 10^{-3} M Cl and (c) 1 M $HClO_4$ + 10^{-2} M Cl.

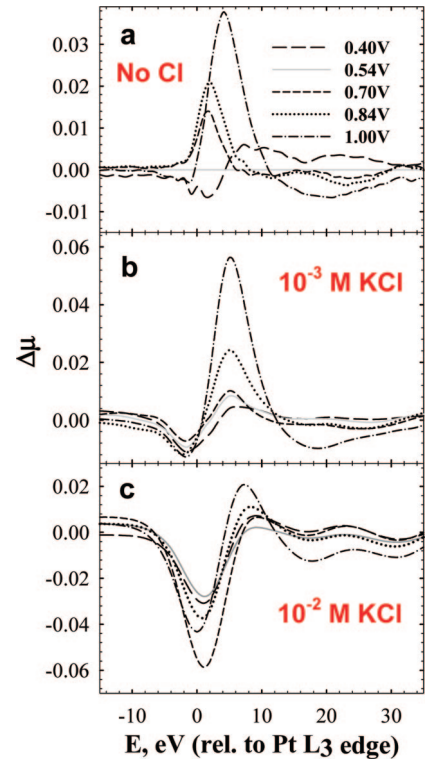

Figure 6. Pt L_3 edge $\Delta\mu = \mu(V, x\text{M } Cl^-) - \mu(0.54\text{ V clean})$ spectra for 30 wt % Pt/C in 1 M $HClO_4$ and the indicated KCl concentrations.

potentials investigated. Also noticeable is an apparent change in the H_2O activation pathway as evidenced by the location of the Pt−O[H] maxima. As mentioned above, a clean Pt surface should undergo Pt−O[H] formation by the transition of $\Delta\mu$ peaks to higher eV values as in Figure 6a and ref 27. This, however, is not observed with 10^{-3} M Cl. Not only do all the $\Delta\mu$ peaks shift to a higher energy position, they also 'stack' on top of each other in Figure 6b, representing a deviation from the normal H_2O activation pathway. Also, the positive maxima in the $\Delta\mu$ spectra between 0.54 to 0.70 V exhibit virtually no increase in magnitude (i.e., Pt−OH suppression in that potential range). Conversely, there is significant growth in the $\Delta\mu$ from 0.7 to 0.84 V, indicating Pt−O[H] formation in agreement with observations from the CV in Figure 2. Between 0.54 and 0.7 V, no appreciable increase in current density was observed, however; at 0.84 V there is a small but discernible Pt−O[H] current in the CV. It is also worth mentioning that the $\Delta\mu$ magnitudes for 0 and 10^{-3} M Cl^- at 0.84 V are quite close indicating the O[H] coverage is approximately equal even though the adsorption process may have occurred differently. The $\Delta\mu$ magnitudes at 1.0 V do not correlate as closely for reasons which will be discussed in the FEFF 8.0 analysis.

In the presence of 10^{-2} M Cl^- (Figure 6c) an overwhelming negative contribution dominates the spectrum at all potentials. In the following 5−10 eV region where the O[H] peak typically appears, only a very small peak is obtained at 1.0 V, indicating little, if any O[H] adsorption occurs. This again is confirmed by inspection of the CV in Figure 2. The small bump on the anodic sweep is almost nonexistent in 10^{-2} M Cl^- at 0.84 V, and at 1.0V only a miniscule current density is achieved. This dip in the $\Delta\mu$ spectra for 10^{-3} and 10^{-2} M Cl^- seems to suggest the line shape for Cl^- adsorption is a negative peak near the

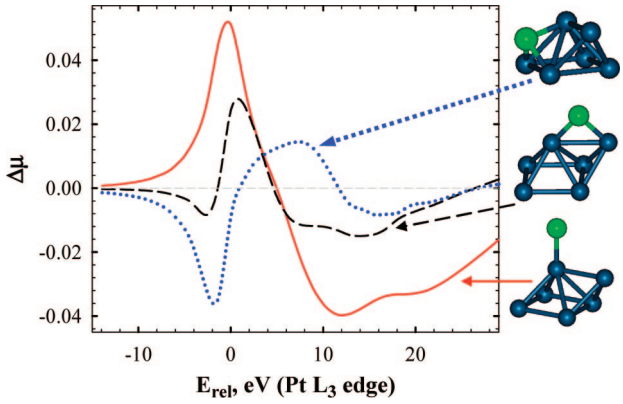

Figure 7. Theoretical $\Delta\mu = \mu(Pt_6{-}Cl) - \mu(Pt_6)$ signatures for atop (solid), bridged (dashed) and 3-fold fcc (dotted) chloride on Pt_6 clusters.

edge; however, definitive adsorption site conclusions cannot be made until theoretical simulations by FEFF 8.0 are discussed below.

FEFF 8.0 Results: Cl^- Binding Site Determination. Figure 7 illustrates the theoretical $\Delta\mu$ spectra for Cl^- adsorbed on a Pt_6 cluster in atop, bridged and 3-fold face-centered-cubic (fcc) configurations as calculated by eq 2. The atop line features a large positive peak near 0 eV and going negative for the remainder of the energy region of relevance. The bridge bonded line contains a less intense positive component shifted slightly higher in energy (~1 eV) with respect to the atop line. It also features a small dip which precedes the positive peak. The 3-fold spectrum reveals a significant negative dip and a broad positive component immediately following, which closely resembles the line shapes obtained in 10^{-2} M Cl^-. In order to understand the effect of Cl^- adsorption in the competing environment of water activation (formation of oxides), Figure 8a shows the theoretical signals derived from 3-fold Cl^- adsorption and that for the corresponding oxides. In addition a composite theoretical signal is shown which combines both these theoretical signatures. Figure 8b provides an overlay plot of 10^{-2} M Cl^- scans with the 3-fold Cl^- theory (for clarity only 0.54 and 1.00 V scans are provided). It is evident from the line shape that 10^{-2} M Cl^- closely resembles the 3-fold bonded Pt−Cl at all probed potentials. This strongly suggests that chloride adsorbs on platinum primarily in 3-fold sites at all potentials and both concentrations.

In the case of 10^{-3} M chloride the adsorption geometry is not as obvious as it was in 10^{-2} M Cl^-. The theoretical $\Delta\mu$ line shapes suggest bridge bonded adsorption; however, we interpret the spectra to be a combination of H_2O activation (hence presence of surface oxides) and 3-fold Cl^- adsorption occurring concurrently. There is direct evidence of both chloride and O[H] adsorption in the $\Delta\mu$. To illustrate this, Figure 8a shows the FEFF 8.0 $\Delta\mu$ simulations for 3-fold O and 3-fold Cl^- with boxes to emphasize the major elements of each adsorbing species. Both Pt_6 clusters show 3-fold adsorption of chloride and O[H] with vastly different $\Delta\mu$ signatures. The dash-dot line, showing the sum of 3-fold $\Delta\mu$ theory exhibits an astonishing likeness to the experimental data in 10^{-3} M chloride. This is, in our opinion, the best evidence indicating 3-fold chloride adsorption occurring in parallel with 3-fold O[H] formation.

The 0.4−0.7 V Region. Perhaps the most interesting potential region in Figure 5 lies between 0.40 and 0.84 V. This region is scrutinized in greater detail because it is within the operating range of most fuel cells and therefore is as significant as the

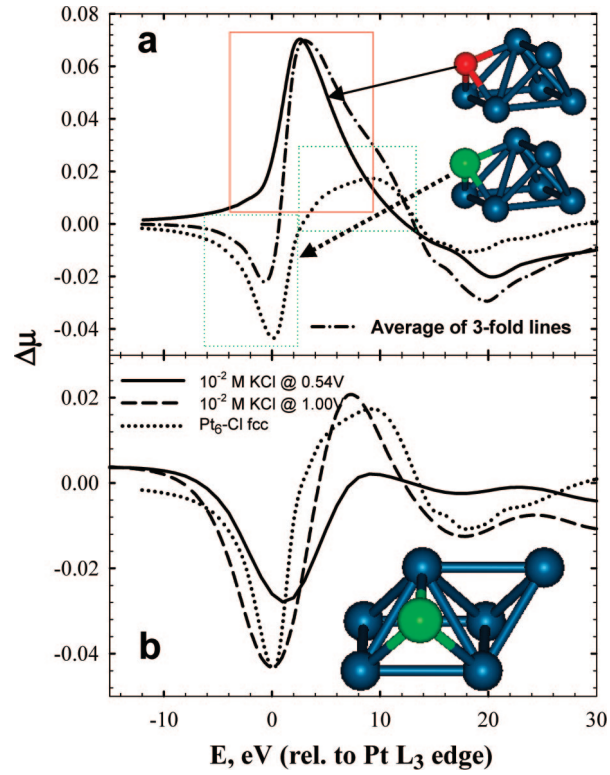

Figure 8. (a) Comparison of theoretical 3-fold O (solid) and 3-fold Cl (dotted) $\Delta\mu$ signatures. The dash-dot line shows the sum of the two curves. (b) Comparison of experimental $\Delta\mu$ in 10^{-2} M Cl^- at 0.54 V (solid), 10^{-2} M Cl^- at 1.00 V (dashed) and theoretical $\Delta\mu$ signature for 3-fold Cl^-.

region at higher potentials. This potential region is where adsorption and rearrangements occur in the Cl^- overlayer. Further, it is the potential region where the more reactive Pt (100) planes plus the corners, steps and edges catalyze water activation and become covered with OH. We discuss Cl^- adsorption and water activation in separate sections below.

Chloride Adsorption and Rearrangement. It is reasonable to estimate relative surface Cl^- coverage changes based on the $\Delta\mu$ peak amplitudes as was done previously,[26,27] even though absolute monolayer coverage values are much more difficult to obtain. In Figure 9 we use the absolute value of the negative going $\Delta\mu$ located near 1 eV as it has been shown to reflect 3-fold Cl^-. The $\Delta\mu$ at potentials less than 0.40 V were excluded here as the Pt−H and Pt−Cl $\Delta\mu$ signatures are too similar, making them impossible to distinguish. Figure 9 also includes previously published data[57] estimating Br coverage on a single crystal Pt (111) face in 0.01 M Br, the Pt−Cl Gibbs free energy (ΔG_{PtCl}) reflecting the Pt−Cl bond strength as well as the EXAFS N_{Pt-Pt} results from Figure 5. Although a similar plot of Cl^- coverage would be preferable, we are not aware of such data, although Lucas et al.[17] have reported the coverage of Cl^- on Pt(111) at 0.25 and 0.7 V as indicated in Figure 9. Note the dramatic increase in Br coverage exactly in the region where the adsorbed H is known to leave. This is entirely consistent with our reduced N_{Pt-Pt} values as noted in Figure 5, and significant increase in $\Delta\mu$ magnitude already evident at 0.4 V as shown. Above 0.25 V, the Br coverage continues to increase with potential but at a much slower rate, and this is believed to occur because of a "continuous compression of the Br adlayer" producing a partially disordered or incommensurate adlayer on the Pt(111) surface,[5] occurring in the region between 0.30 and 0.55 V. Such compression will move some of the halide ions into bridged and atop sites. This is the probable cause for the

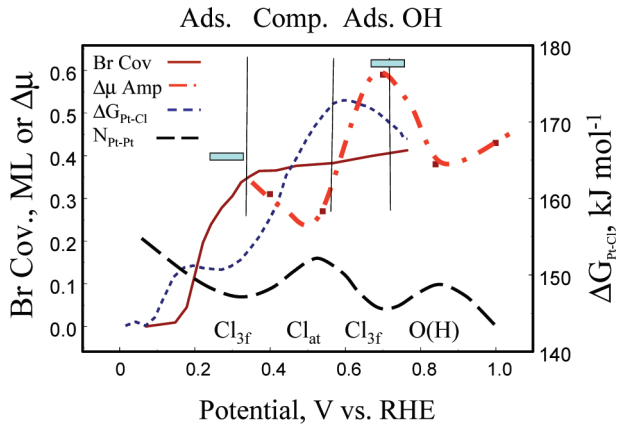

Figure 9. Plot of Br coverage[57] and $\Delta\mu$ amplitudes representing Cl^- coverage (this work) using left axis, and the Gibbs free energy for Cl^- adsorption[14] using the right axis. The Pt−Pt coordination numbers from Table 2 for the 10^{-2} M Cl^- case are indicated with arbitrary units and the $\Delta\mu$ amplitude has been scaled so that it approximately represents coverage in ML. The small shaded lines indicate Cl^- coverage at 0.25 and 0.70 V as estimated by Lucas et al.[17] The vertical lines roughly separate the regions where Cl^- adsorption, compression in the Cl^- overlayer, more Cl^- adsorption, and OH adsorption dominate as indicated. The symbols at the bottom indicate the dominant $\Delta\mu$ signatures from Figure 10 in each region.

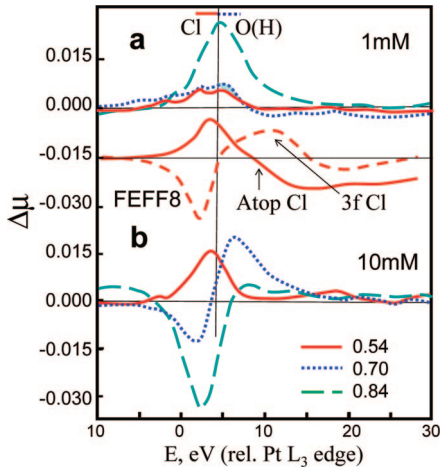

Figure 10. Plot of $\Delta\mu = \mu(V) - \mu(0.40\ V)$ for the indicated Cl^- concentrations and comparison with FEFF 8.0 results from Figure 6. Vertical line separates the energy where below the atop Cl^- $\Delta\mu$ signature dominates and above the O[H] dominates in magnitude.

reduction in apparent Cl^- coverage as suggested by the $\Delta\mu$ results between 0.3 and 0.5 V. Note that in Figure 7, the FEFF 8.0 results show that atop/bridged Cl^- does not have the large negative feature around 1 eV, so the movement of 3-fold Cl into atop/bridged sites will decrease this negative contribution even though additional Cl^- might be adding to the surface. Above 0.55 V, apparently more Cl^- is added again as suggested by the $\Delta\mu$ magnitudes, and the results of Lucas et al.[17] shown in Figure 9. The 'hump' in N_{Pt-Pt} between 0.4 and 0.7 V is now easily understood. Recall as mentioned above that 3-fold Cl reduces N_{Pt-Pt} and atop Cl will increase it, just as we see for O[H] and O. Thus the increase in N_{Pt-Pt} falls right in the 'compression' region, and the decrease again during the second Cl adsorption zone. Thus, the $\Delta\mu$ and changes in N_{Pt-Pt} from EXAFS analysis correlate very well.

Figure 9 also shows that the Pt−Cl Gibbs free energy reaches a maximum right where the Cl^- coverage begins to increase again. The increase in ΔG_{Pt-Cl} apparently arises because of the increasing charge on the Pt surface atoms with potential. The decrease in ΔG_{Pt-Cl} above 0.5 V is believed to arise because of additional Cl^- adsorption, which increases the repulsive lateral interactions and hence reducing the net Pt−Cl bond strength. Other studies[5,15] have also shown that Cl^- adsorbs following H desorption and concurrently or slightly before O[H] adsorption. The decrease in Cl^- coverage as indicated by the $\Delta\mu$ above 0.7 V, obviously arises because of O[H] adsorption.

To further investigate the Cl^- rearrangement from 3-fold into atop sites during the Cl^- adlayer compression stage, a set of $\Delta\mu$ spectra are given in Figure 10, only this time using 0.40 V *in the same electrolyte* as the reference spectrum (e.g., $\Delta\mu = \mu(x\text{V}, 10^{-3}\ \text{M}\ Cl^-) - \mu(0.4\text{V}, 10^{-3}\ \text{M}\ Cl^-)$). If atop Cl^- adsorption is indeed occurring, it should be apparent by isolating such a $\Delta\mu$ signature in this potential region by eliminating the large contribution from the 3-fold Cl^- that has adsorbed below 0.4 V. In the case of 10^{-2} M Cl^- (Figure 10b), the $\Delta\mu$ signature clearly indicates the addition of atop Cl^- at 0.54 V and 3-fold Cl^- at 0.70 V. This is again consistent with our discussion of Figure 9. The line shape at 0.84 V reflects the adsorption of O[H] along with a small amount of additional Cl^-.

Examination of Figure 10a for the 10^{-3} M Cl^- is also revealing. The $\Delta\mu$ spectra at 0.54 and 0.70 V reflect primarily atop Cl^- combined with some atop O[H]. The signature for atop Cl^- and O[H] are very similar, but that for atop Cl^- is shifted to lower energy by approximately 5 eV. This is confirmed by the comparison of the $\Delta\mu$ signature from Figure 10b for 10^{-2} at 0.54 V, which is believed to reflect entirely atop Cl^- without any adsorbed O[H]. One can then detect a small amount of O[H] present at 0.70 V in 10^{-3} M Cl^- (shaded area in Figure 10a) that is not present at 0.54 V. This also explains the large amplitudes of the $\Delta\mu$ signatures in Figure 6b for the 10^{-3} M Cl^-; amplitudes larger than those in Figure 6a without Cl^-. Seemingly both atop Cl^- and O[H] are adsorbing together at all potentials above 0.54 V. Comparison of the CVs in Figure 2 and the N_{Pt-Pt} curves in Figure 5 both show that even the 10^{-3}M Cl^- has a harmful effect on the adsorption of OH below 0.8 V, so indeed we suspect that the $\Delta\mu$ curves in Figure 6a reflect primarily atop Cl^-, not O[H] (the one at 0.84 V may reflect about equal amounts of each). Further, since the N_{Pt-Pt} changes well below 0.84 V reflects adsorption more at the corners/edges than on the Pt(111), this indeed provides evidence that O[H] cannot displace Cl^- at the corners/edges until about 200 mV higher than normal, just as on the Pt(111) planes.

Water Activation on Low Index Pt Planes, Corners and Edges. Previous studies[10] regarding Cl^- adsorption on larger Pt clusters as summarized in Figure 11 shed light on the interplay between O[H] and Cl^- on the different cluster planes. In pure 1 M $HClO_4$, and in 1 M $HClO_4$ + 10^{-2} M Cl^-, the CVs reveal a feature in the 0.4−0.7 V region. Note that the Pt/C electrocatalysts in Figure 11 have an average particle size of 30 Å, which according to correlation with the Benfield[49] cuboctahedron model indicates significant presence of Pt(100) sites (Table 2). Since the Pt−Cl interaction on lower coordinated Pt atoms at the corners and edges, as well as on the more open Pt(100) surface, is known to be stronger than on the Pt(111) faces,[5] these more reactive sites are expected to be covered with Cl^- well below 0.70 V. However, also note that the second rise in the CV, beyond 0.70 V, does not occur until higher potentials in the presence of 10^{-3} M Cl^-. It should be apparent that OH can displace Cl^- on the Pt (100) faces and corners/edges but not so easily on the Pt(111) faces.

Also shown in Figure 11, the production of H_2O_2, which occurs when the O_2 dissociation is partially obstructed forcing it to adsorb end-on, sharply increases in the 0.4−0.7 V region

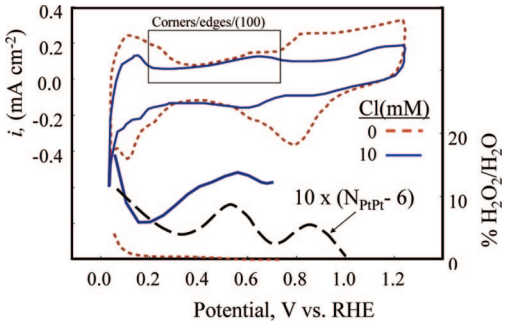

Figure 11. Cyclic voltammograms of 20 wt % Pt/C (*E-TEK*) in 0.5 M $HClO_4$ and 0.5 M $HClO_4$ + 10^{-2} M Cl^- as reported by Schmidt et al.[10] (50 mV s^{-1}, 900 RPM, 7 μgPt cm^{-2}). Also shown are fraction of H_2O_2 formed during ORR on these same samples (E_{ring} = 1.2 V, 5 mV s^{-1}, 1600 RPM) as reported by Schmidt et al.[10] Finally the N_{Pt-Pt} data from Table 2 are plotted scaled and shifted as noted to fit on the right axis. Rectangle indicates region where O[H] from water activation occurs on the cluster corners/edges and on the Pt(100) planes.

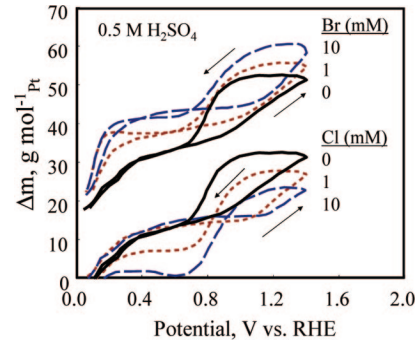

Figure 12. Adsorbate mass change (from that at 0.0 V) with potential as estimated from EQCN data reported by Zolfaghari et al.[46] in 0.5 M H_2SO_4 and the indicated concentrations of Br^- or Cl^-. Arrows indicate anodic/cathodic potential direction. The data for Br have been shifted up by 20 g mol^{-1} Pt for clarity.

when compared with the absence of Cl^-. This indicates that OH coming from water activation can displace Cl^- on the Pt sites such as Pt (100) but O_2 during ORR cannot.

Figure 11 also shows N_{Pt-Pt} for the 10^{-2} M Cl^- concentration from Figure 5 to emphasize the different behavior between N_{Pt-Pt} and the CV in this region where the feature is much broader. Therefore, we conclude that O[H] adsorbing on the corners/edges and Pt(100) sites in this region in 10^{-2} M Cl^- is not believed to be the cause of the 'hump' in N_{Pt-Pt}, but rather the compression of the Cl^- adlayer on the Pt(111) faces and corners/edges as discussed above.

Interplay of Bisulfate and Halide Ions on Pt. The results above reveal the interaction between adsorption of O[H] and Cl^- and its dependence on the Pt adsorption site. A comparative study of the interplay between other anions can provide further insight. Here, we will extend our findings with some recently published results[46] to understand the complex scenario of competing adsorption among other commonly found anions. Of particular interest are some recent findings involving Cl^- and Br poisoning of Pt surfaces in both $HClO_4$ and H_2SO_4. While studies performed in H_2SO_4 are disadvantageous in the sense that the problem is complicated due to bisulfate adsorption, they nevertheless furnish information on how bisulfate behaves in an environment containing both Cl^- and O[H]. Although these results are by no means new, it is our intent to offer an alternative interpretation than that offered by Zolfaghari et al.[46] as their paper made no mention of bisulfate adsorption throughout their discussion. Figure 12 shows a recreation of electrochemical quartz crystal nanobalance (EQCN) results from their experiments involving Cl^- and Br adsorption in H_2SO_4. The representation of the data we present is different from that in their manuscript for the sake of clarity. Two sets of curves are shown indicating the mass-frequency response in H_2SO_4, used here for a standard/reference, with that in the presence of Cl^- and Br under various concentrations. Sulfuric acid furnishes bisulfate ions that adsorb weakly on the surface and thus should be expected to increase the mass density of adsorbate. The onset of oxide formation is indicated by a change of slope in the curve, and occurs around 0.80 V. In the presence of chloride, we observe that as the concentration of chloride in solution increases, the amount of total mass on the surface *decreases*. This can only occur as a result of bisulfate anion desorption.

For the ensuing discussion, the following approximations are made with respect to mass density. The mass of adsorbate/mol Pt-atom is approximately 18 for O^{2-}/OH^-, 50 for HSO_4^-, 36 for Cl^- and 80 for Br^-. These mass densities assume one Cl^- and one Br anion per surface Pt, 1/2 bisulfate per Pt atom, and 1.5 O per Pt. The results can then easily be accounted for by assuming Cl^-, which has a smaller mass density, adsorbs more strongly than bisulfate. Thus, on displacing bisulfate, the overall mass decreases with increasing Cl^- concentration, as the heavier bisulfate leaves the surface for the lighter, more strongly bound chloride ions. Since Br ion is heavier, the mass density increases with Br concentration. These curves clearly indicate that not all of the halide anions are displaced from the surface by O even at 1.4 V, because if that were the case, the resulting curves at 1.4 V should fall at the same place with whatever the O mass density was at that point. Some disagreement on this point has occurred in the literature;[46] however, Figure 12 makes clear that the halides remain in part on the surface all the way up to 1.4 V.

Figure 12 reveals a very interesting difference between Br and Cl^- adsorption relative to the bisulfate; Cl^- shows a hystersis effect in the region between 0.3 and 0.8 V, while Br does not. In the case of the Cl^-, during the anodic sweep the mass density is independent of the Cl^- concentration which indicates that bisulfate is on the surface. However, during the cathodic sweep the mass density changes as expected with Cl^- concentration suggesting the presence of Cl^- ion. The adsorption of a bisulfate/water adlayer is known to give rise to the "butterfly" feature in CV curves Pt(111) single crystals. Apparently, Cl^- is not able to penetrate this adlayer until it is disrupted by O adsorption at higher potentials. Then, during the cathodic sweep the Cl^- ions readsorb and bisulfate is not able to displace the adsorbed Cl^-. This effect seemingly does not occur in mixed Br/H_2SO_4 electrolytes as Br adsorption occurs so strongly that it can displace the bisulfate either way.

This interpretation of EQCN data also calls into question the conclusions reached more recently by Yadav et al.[58] They report similar EQCN results for halide ions in H_2SO_4. They also report analogous hysteresis effects in the case of Cl^- and attributed it to Pt dissolution. While we cannot rule out some Pt dissolution during potential cycling, clearly the effects of bisulfate adsorption should not be ignored; otherwise the extent of Pt dissolution can be grossly overestimated.

Summary and Conclusions

The combination of in situ X-ray absorption spectroscopy, and electrochemical measurements (CV and RDE), and previously published EQCN data has provided further understanding of the nature of chloride poisoning on different faces/sites of

TABLE 3: Summary of Results at Different Faces and Corner/Edge Sites on Pt Particles

adsorbate species	corners/edges	Pt(100) faces	Pt(111) faces
OH potential region	0.4−0.7	0.4−0.7 V	>0.7 V
OH from H_2O activation	threshold pot. moved up by 200 mV in Cl	not affected by Cl	threshold pot. moved up by 200 mV in Cl
ORR	site blocked by Cl	Cl enhances 2e over 4e red.	site blocked by Cl
bisulfate	expected to have little effect on Cl ad.	appears to have little effect on Cl	bisulfate adlayer blocks Cl adsorption anodically; no effect cathodically
apparent ion adsorption preference	Br > Cl > OH > HSO_4	OH> Cl >HSO_4	Br > HSO_4 > Cl >OH

platinum catalysts in acidic medium ($HClO_4$). The sensitivity to anion adsorption effects of the $\Delta\mu$ XANES procedure is clear. In this work, Cl^- ions produced a direct contribution to the $\Delta\mu$ in contrast to that found previously for bisulfate which did not appear in the $\Delta\mu$, unless OH or other adsorbates were coadsorbed on the surface to force the bisulfate anions into site-specific binding.

To the best of our knowledge, this is the first study to provide conclusive evidence for the site-specific 3-fold adsorption of chloride species on Pt(111) faces in a working fuel cell environment, though the compression of the Cl^- adlayer, which apparently forces some Cl^- into atop/bridge sites between 0.40 and 0.55 V, also occurs. The adsorbed chloride on the Pt(111) faces at the investigated concentrations (10^{-3} and 10^{-2} M) are believed to be adsorbed in equilibrium; i.e., $Cl^- + Pt \rightarrow Cl^-/Pt$ at nearly all potentials consistent with our $\Delta\mu$ results and Figure 9. At 10^{-2} M halide concentration, the coverage at 0.3V appears to be around 0.35−0.4 ML for both Br and Cl^-. This probably occurs because at this low potential the halide ions are still highly negatively charged, so that the large Coulomb lateral interactions keep the coverage small in both cases. As the magnitude of the halide ion charge decreases with potential, the Coulombic lateral interactions decrease, enabling some compression of the adlayers. In the case of the Cl^-, the smaller covalent radius then enables a great deal more 3-fold Cl^- to adsorb between 0.5 and 0.7 V; in Br this apparently cannot occur because of the much larger covalent radius.

Somewhat surprisingly, N_{Pt-Pt} found from the EXAFS analysis is also quite dependent upon Cl^- adsorption. Chloride adsorption into the 3-fold sites decreases N_{Pt-Pt}, similar to that found previously for 3-fold O adsorption,[27] and clearly arises because of the proximity of the Cl^- anion partially in between the Pt atoms. In contrast, atop Cl^- adsorption increases N_{Pt-Pt}, and rearrangement of some Cl^- atoms into atop sites between 0.40 and 0.55 V is therefore also evident from N_{Pt-Pt}. The change of N_{Pt-Pt} with potential therefore reveals the nature of the adsorption, atop vs 3-fold Cl^- and O[H].

The interplay of anionic (Cl^-, Br^-, OH^-, and HSO_4^-) adsorption on the different surfaces of Pt are indeed complex as the results summarized in Table 3 indicate. For example, we find that O[H] can displace atop chloride on the Pt(100) faces, but not on the Pt(111) faces as well as corners and edges until much higher potentials than without chloride. Chloride also drastically alters the ORR causing an increase of the overpotential by approximately 85 mV for every 10-fold increase in Cl^- concentration with a total 150−200 mV increase in the overpotential at large concentrations at the Pt(111) sites. In contrast, Cl^- appears to force the ORR to the undesirable 2-electron reduction (peroxide production) at the corner/edge sites. It is well-known that peroxide production occurs when the nearby surface is crowded thus making it difficult for the O_2^- intermediate to "tip over" and result in dissociation of the O_2 bond.

Although we did not directly study bisulfate adsorption in this work, a reinterpretation of the EQCN results shed further light on the interplay between Cl^- and Br vs bisulfate. It seems obvious that Cl^- ions cannot displace the bisulfate−water adlayer formed on Pt(111) planes after it is formed at lower potentials, however, once the bisulfate is disturbed at higher potentials, it cannot displace the adsorbed Cl^-. On the other hand the Br ion is able to displace bisulfate at lower potentials in the anodic direction.

The relative order of the Pt−X adsorption preferences indicated in Table 3 at the different binding sites is suggested by the results and discussion above as well as previous results summarized by Markovic et al.[5] They should be taken as only very qualitative and phenomenological, but they do give some insight into the complex interplay of anion adsorption occurring at different sites in an electrochemical cell. Markovic et al.[5] concluded that on nearly all low-index surfaces the adsorbate-Pt interactions increase in the order HSO_4 < Cl < Br. They further indicated that for the halides the Pt-X interaction was stronger on the Pt(100) faces than on the Pt(111) faces, but that the bisulfate interactions went in the opposite direction (Pt(111) < Pt(100)). In contrast, the EQCN results suggest that the Pt−bisulfate interaction is in fact stronger than the Pt−Cl on the Pt(111) faces. Further, although both the Pt−halide and Pt−OH interactions are stronger on the corners/edges and Pt(100) sites than on the Pt(111) sites, the difference is much stronger for the Pt−OH interaction (70−80 kJ mol^{-1})[5] so that of the adsorbates studied, the Pt−OH interaction is apparently the strongest on the Pt(100) faces, and the weakest on the Pt(111) faces while intermediate on the corners/edges.

These relative interaction strengths indicated here should help to explain the different dependencies of the important ORR reaction on anion adsorption, and suggests that the effect of Cl^- poisoning might be quite dependent on the particle size, as the relative number of corner/edge sites to Pt (111) face sites changes with particle size. Markovic et al.[5] have already given an extensive review of some these effects on low index single crystal faces, but not on real nanoparticle-sized catalysts.

Acknowledgment. Financial support for this effort was provided by the Army Research Office via both a single investigator grant and a Multi University Research Initiative (Case Western Reserve University, P.I.). B.S. acknowledges financial support by way of a Summer Research Fellowship award towards part of this study from the Sigma Xi foundation. The authors are grateful for the use of X11-B at the National Synchrotron Light Source, Brookhaven National Laboratory, Upton NY, which is supported by the U.S. Department of Energy, Office of Science, Office of Basic Energy Sciences, under Contract No. DE-AC02-98CH10886.

References and Notes

(1) Gottesfeld, S.; Zawodzinski, T. A. *Adv. Electrochem. Sci. Eng.* **1997**, *5*, 195.

(2) Breiter, M. W. *Electrochim. Acta* **1963**, *12*, 925.

(3) Horanyi, G.; Rizmayer, E. M. *J. Electroanal. Chem. Interfacial Electrochem.* **1977**, *83*, 367.

(4) Huang, J. C.; O'Grady, W. E.; Yeager, E. *J. Electrochem. Soc.* **1977**, *124*, 1732.
(5) Marković, N. M.; Ross, P. N. *Surf. Sci. Rep.* **2002**, *45*, 117.
(6) Markovic, N.; Gasteiger, H.; Ross, P. N. *J. Electrochem. Soc.* **1997**, *144*, 1591.
(7) Slygin, A.; Frumkin, A. *Acta Physicochim. S.S.S.R.* **1935**, *3*, 791.
(8) Llopis, J. *Catal. Rev.* **1968**, *2*, 161.
(9) Bagotzky, V. S.; Vassilyev, Y. B.; Weber, J.; Pirtskhalava, J. N. *J. Electroanal. Chem.* **1970**, *27*, 31.
(10) Schmidt, T. J.; Paulus, U. A.; Gasteiger, H. A.; Behm, R. J. *J. Electroanal. Chem.* **2001**, *508*, 41.
(11) Wang, J. X.; Markovic, N. M.; Adžić, R. R. *J. Phys. Chem. B* **2004**, *108*, 4127.
(12) Zhang, L.; Mukerjee, S. *J. Electrochem. Soc.* **2006**, *153*, A1062.
(13) Lane, R. F.; Hubbard, A. T. *J. Phys. Chem.* **1975**, *79*, 808.
(14) Li, N.; Lipkowski, J. *J. Electroanal. Chem.* **2000**, *491*, 95.
(15) Markovic, N.; Ross, P. N. *J. Electroanal. Chem.* **1992**, *330*, 499.
(16) Campbell, D. J.; Lynch, M. L.; Corn, R. M. *Langmuir* **1990**, *6*, 1656.
(17) Lucas, C. A.; Marković, N. M.; Ross, P. N. *Phys. Rev. B* **1997**, *55*, 7964.
(18) Mukerjee, S.; McBreen, J. *J. Electrochem. Soc.* **1999**, *146*, 600.
(19) Mukerjee, S.; McBreen, J.; Reilly, J. J.; Johnson, J. R.; Adzic, G.; Petrov, K.; Kumar, M. P. S.; Zhang, W.; Srinivasan, S. *J. Electrochem. Soc.* **1995**, *142*, 2278.
(20) O'Grady, W. E.; Ramaker, D. E. *Electrochim. Acta* **1998**, *44*, 1283.
(21) Koningsberger, D. C.; Mojet, B. I.; Van Dorssen, G. E.; Ramaker, D. E. *Top. Catal.* **2000**, *10*, 143.
(22) Koningsberger, D. C.; Mojet, B. L.; Miller, J. T.; Ramaker, D. E. *J. Synchrotron Radiat.* **1999**, *6*, 135.
(23) Koningsberger, D. C.; Mojet, B. L.; van Dorssen, G. E.; Ramaker, D. E. *Top. Catal.* **2000**, *10*, 143.
(24) Ramaker, D. E.; Mojet, B. L.; Koningsberger, D. C.; O'Grady, W. E. *J. Phys.: Condens. Matter* **1998**, *10*, 8753.
(25) Murthi, V. S.; Urian, R. C.; Mukerjee, S. *J. Phys. Chem. B* **2004**, *108*, 11011.
(26) Teliska, M.; Murthi, V. S.; Mukerjee, S.; Ramaker, D. E. *J. Electrochem. Soc.* **2005**, *152*, A1259.
(27) Teliska, M.; O'Grady, W. E.; Ramaker, D. E. *J. Phys. Chem. B* **2005**, *109*, 8076.
(28) Teliska, M.PhD. *Dissertation. Ph.D.*, The George Washington University, 2004.
(29) Teliska, M.; O'Grady, W. E.; Ramaker, D. E. *J. Phys. Chem. B* **2004**, *108*, 2333.
(30) Teliska, M.; Murthi, V. S.; Mukerjee, S.; Ramaker, D. E. *J. Phys. Chem. C* **2007**, *111*, 9267.
(31) Scott, F. J.; Mukerjee, S.; Ramaker, D. E. *J. Electrochem. Soc.* **2007**, *154*, A396.
(32) Ziegelbauer, J. M.; Gatewood, D.; Gullá, A. F.; Ramaker, D. E.; Mukerjee, S. *Electrochem. Solid-State Lett.* **2006**, *9*, A430.
(33) Arruda, T. M.; Shyam, B.; Ziegelbauer, J. M.; Ramaker, D. E.; Mukerjee, S. *ECS Trans.* **2007**, *11*, 903.
(34) Ramaswamy, N.; Hakim, N.; Mukerjee, S. *Electrochm. Acta* **2008**, *53*, 3279.
(35) McBreen, J.; O'Grady, W. E.; Pandya, K. I.; Hoffman, R. W.; Sayers, D. E. *Langmuir* **1987**, *3*, 428.
(36) Newville, M. *J. Synchrotron. Radiat.* **2001**, *8*, 322.
(37) Newville, M.; Livins, P.; Yacoby, Y.; Stern, E. A.; Rehr, J. J. *Phys. Rev. B* **1993**, *47*, 14126.
(38) Ramaker, D. E.; Mojet, B. L.; Miller, J. T.; Koningsberger, D. C. *Top. Catal.* **2000**, *10*, 157.
(39) van Dorssen, G. E.; Koningsberger, D. C.; Ramaker, D. E. *J. Phys.: Condens. Matter* **2002**, *14*, 13529.
(40) Janin, E.; von Schenck, H.; Göthelid, M.; Karlsson, U. O. *Phys. Rev. B* **2000**, *61*, 13144.
(41) Stamenkovic, V.; Marikovic, N. M.P. N; Ross, J. *J. Electroanal. Chem.* **2001**, *500*, 44.
(42) Li, N.; Lipkowski, J. *J. Electroanal. Chem.* **2000**, *2000*, 95.
(43) Marković, N. M.; Gasteiger, H. A.; Grgur, B. N.; Ross, P. N. *J. Electroanal. Chem.* **1999**, *467*, 157.
(44) Stamenković, V.; Marković, N. M.; Ross, P. N. *J. Electroanal. Chem.* **2001**, *500*, 44.
(45) Jerkiewicz, G.; Vatankhah, G.; Lessard, J.; Soriaga, M. P.; Park, Y.-S. *Electrochim. Acta* **2004**, *49*, 1451.
(46) Zolfaghari, A.; Conway, B. E.; Jerkiewicz, G. *Electrochim. Acta* **2002**, *47*, 1173.
(47) Ramaker, D. E.; Oudenhuijzen, M. K.; Koningsberger, D. C. *J. Phys. Chem. B* **2005**, *109*, 5608.
(48) Kinoshita, K. *J. Electrochem. Soc.* **1990**, *137*, 845.
(49) Benfield, R. E. *J. Chem. Soc. Faraday Trans.* **1992**, *88*, 1107.
(50) Hardeveld, R. v.; Hartog, F. *Surf. Sci.* **1969**, *15*, 189.
(51) Hardeveld, R. v.; Monfoort, A. V. *Surf. Sci.* **1969**, *4*, 396.
(52) Stonehart, P. *Bur. Bunsenges Phys. Chem.* **1990**, *94*, 913.
(53) Mukerjee, S.; McBreen, J. *J. Electroanal. Chem.* **1998**, *448*, 163.
(54) Balbuena, P. B.; Altomare, D.; Vadlamani, N.; Bingi, S.; Agapito, L. A.; Seminario, J. M. *J. Phys. Chem. A* **2004**, *108*, 6378.
(55) Xu, Y.; Ruban, A. V.; Mavrikakis, M. *J. Am. Chem. Soc.* **2004**, *126*, 4717.
(56) Fiebelman, P. J. *J. Phys. Rev. B* **1996**, *77*, 2257.
(57) Garcia-Araez, N.; Climent, V.; Herrero, E.; Feliu, J.; Lipkowski, J. *J. Electroanal. Chem.* **2005**, *576*, 33.
(58) Yadav, A. P.; Nishikata, A.; Tsuru, T. *Electrochim. Acta* **2007**, *52*, 7444.

JP8067359